Stoichiometric Carbocatalysis *via* Epoxide-like C−S−O Configuration on Sulfur-Doped Biochar for Water Remediation

Zhonghao Wan[1], Zibo Xu[1], Yuqing Sun[1], Qiaozhi Zhang[1], Deyi Hou[2], Bin Gao[3], Eakalak Khan[4], Nigel Graham[5], Daniel C.W. Tsang[1, 6 *]

[1] Department of Civil and Environmental Engineering, The Hong Kong Polytechnic University, Hung Hom, Kowloon, Hong Kong, China.

[2] School of Environment, Tsinghua University, Beijing 100084, China.

[3] Department of Agricultural and Biological Engineering, University of Florida, Gainesville, FL 32611, United States.

[4] Department of Civil and Environmental Engineering and Construction, University of Nevada, Las Vegas, NV 89154, USA.

[5] Department of Civil and Environmental Engineering, Imperial College London, South Kensington Campus, London SW7 2AZ, United Kingdom.

[6] Research Centre for Resources Engineering towards Carbon Neutrality, The Hong Kong Polytechnic University, Hung Hom, Kowloon, Hong Kong, China.

* Corresponding author: dan.tsang@polyu.edu.hk

ABSTRACT

Heteroatom doping is a promising technique to enhance biochar for effective environmental remediation. However, development of electroactive heteroatom-doped biochars, *e.g.*, sulfur-doped biochar, has been hindered due to complex nature of non-stoichiometric biomass-derived carbon and changeable electrochemical state of dopants. Herein, we produced a series of platform wood-derived biochars with customized levels of minerals and redox-active moieties, aiming to unravel the crucial factors determining sulfur doping. Calcium (Ca) in biochar was found to preferentially coordinate with sulfur to form inactive inorganic sulfur minerals (*i.e.*, $CaSO_4$ and CaS) with inferior catalytic reactivity. After diminishing the inherent Ca minerals beforehand, we could introduce surface phenoxyl-type radicals ($C-O^{\bullet}$) and vacancy defects on the biochar to develop an electrophilic C−S−O bonding configuration, which guaranteed a high affinity towards peroxymonosulfate (PMS, 2.08 mM g^{-1}, 30 min) and efficient removal of bisphenol A (BPA, 91.1%, 30 min). Scavenging experiments and *in-situ* Raman analyses indicated that the epoxide-like C−S−O structure induced nucleophilic addition of PMS to generate surface singlet oxygen ($^1O_2$, major) and hydroxyl radicals ($^{\bullet}OH$, minor) through a preservative and stoichiometric interfacial reaction. Overall, the approach described overcomes the major hurdles in science-informed fabrication of sulfur-doped biochar and advances its development in niche environmental remediation.

Keywords

Carbonaceous catalyst; Heteroatom doping; Persulfate activation; Water remediation; Sustainable waste management.

1. Introduction

In the context of severe water scarcity and widespread pollution, a high-efficacy and easily available catalyst for water body remediation is indispensable to ensure global human health and sustainable resource utilization [1]. Engineered biochar has been recently proposed as a carbocatalyst which emerges as an ideal option owing to its field adaptability, carbon versatility, and economic feasibility. It exploits a resource that otherwise would be treated by open burning or landfilling, which thereby mitigates the generation of greenhouse gases and leachate pollution [2, 3]. In contrast, conventional carbon-based counterparts (*e.g.*, activated carbon, carbon nanotubes, or graphene) usually originate from petrochemical feedstock and require multiple chemical-/energy-consuming synthesis [4]. On this basis, biochar can be considered a superior eco-friendly material for worldwide application to contribute to sustainable developments goals and carbon neutrality, especially in developing countries.

In practical water disinfection, using biochar to activate persulfate (*i.e.*, peroxydisulfate (PDS) and peroxymonosulfate (PMS)) is of considerable interest to the scientific community [5].` Fundamentally, biochar can efficiently coordinate both radical and nonradical persulfate activations to cater for diverse demands under different practical conditions [6, 7]. Although biochar shows a great potential as a green carbocatalyst for persulfate activation, its durability and efficiency are still limited by its nonstoichiometric carbon nature and/or the impeded contact between reactants and active sites [8-10]. To overcome these shortcomings, various metal ions (*e.g.*, Fe, Mg, and Zn) have been extensively investigated as dehydration/pore-forming agents to either create more turbostratic nanostructures or confer denser electron-rich sites [11-14]. However, these large metal centers, anchored by the endogenous mineral contents and oxygen functionalities (OFGs) on biochar *via* weak interactions of ion exchange and hydrogen bonding, would inevitably leach to an uncontrollable extent during redox reactions, and subsequently result in a deteriorated catalytic durability and unintended environmental concerns [7]. Comparatively, non-metal heteroatom doping technology, which confers biochar a polarized electron/spin distribution within heterocyclic units, promises an improved electroactive capacity towards persulfate activation with minimal undesirable side effects [15-17].

In recent years, nitrogen-doped biochar has been increasingly studied, and it shows a great catalytic performance especially in water decontamination [18]. However, excessive thermolysis of nitrogen-containing biomass can release undesirable quantities of nitrogen oxides, which potentially cause photochemical smog and surface ozone pollution. In order to find a more sustainable alternative, researchers have turned to another carbon-compatible and naturally abundant element, sulfur, and demonstrate many intriguing potentials [19]. Wang, Guo, Liu, Si, Luo, Zhao and Ren [20] successfully incorporated sulfur atoms into sludge-derived biochar to achieve a high-performance carbocatalysis. Nonetheless, Ding, Yang, Qian, Chen and Cai [21] reported that the introduction of sulfur exerted negative effects on the catalytic performance of rice straw biochar, probably due to the similar electrochemical property of sulfur (electronegativity: $\chi_S = 2.58$) to that of carbon ($\chi_C = 2.55$), which differed from that of nitrogen ($\chi_N = 3.04$) capable of inducing a polarized dipole moment on biochar [7]. Considering that the sludge-derived biochar consisted of complicated compositions [22], the contradictory results reported might be attributed to critical impacts of its inherent redox-active moieties (RAMs, including OFGs and persistent free radicals (PFRs)). The above results indicate that the doping mechanisms for sulfur (and other heteroatoms) into biochar currently remain in a trial-and-error stage and cannot provide valid guidance for practical applications. Thus, it is necessary and important to unravel the interactions between sulfur and inherent biochar structures, which can enable the science-informed design of biochar doped with diverse heteroatoms for effective pollution control in aqueous systems.

Inherent minerals and RAMs, derived respectively from nutrient uptake and incomplete combustion of biomass [23-25], are two primary reactive components of biochar. Ca minerals and RAMs have potential to alter the chemical states and electronic structures of doped heteroatoms [15, 18, 26]. However, relationships between the specific biochar components and sulfur heteroatoms, ultimate sulfur bonding configurations, and underlying catalytic mechanisms, have yet to be revealed. Therefore, we raised hypotheses that: (i) sulfur with diverse valence states can form various intermediates (*e.g.*, sulfide, sulfate, and oxides) that would interfere with its transformation into dopants; (ii) the minerals and RAMs in biochar play a decisive role in the thermochemical conversion of sulfur due to their different thermodynamic stabilities; and (iii) sulfur speciation (*i.e.*, mineral sulfur and sulfur dopants) influences the catalytic performance, potentially accounting for the mixed results or misinterpretation of experimental observations in previous studies [27].

To test the hypotheses and shed light on the above uncertainties about sulfur-doped biochar and its catalytic mechanisms during water disinfection, we designed a series of biochars with customized levels of minerals and RAMs. Based on the various characterization and experimental techniques, our results demonstrated that sulfur preferentially coordinated with minerals transforming into stable inactive $CaSO_4$ and CaS to impede catalytic performance. By contrast, in the absence of the minerals, sulfur heteroatoms would occupy the vacancy defects adjacent to phenoxy-type PFRs, forming an epoxide-like C−S−O structure in the biochar under a moderate pyrolytic temperature of 500 °C. This C−S−O configuration catalytically induced a nucleophilic addition of peroxide molecules, and subsequently generated abundant singlet oxygen ($^1O_2$) for aqueous pollutant degradation. Overall, this work has revealed the specific sulfur coordination to foster carbocatalysis, thereby advancing the scientific basis for developing an on-demand heteroatom-doped biochar for sustainable water remediation.

2. Materials and Methods

2.1. Chemicals

All the chemicals used in this study were of analytical reagent grade. Detailed information can be found in the **Supplementary Material**, **Text S1**.

2.2. Preparation of Platform Biochars

Samples of local woody yard waste with a marginal sulfur content (< 0.5 wt.%) were obtained from the Environmental Protection Department, Hong Kong, without further purification. Lignin-rich wood is an ideal precursor to synergize with heteroatom doping technology to prepare stable and scalable carbocatalysts [28], while more than 380 tons of wood wastes are sent to municipal landfills daily in Hong Kong. To contribute to the worldwide target of carbon neutrality, the discarded woods would be transformed into value-added biochar for a bioresource utilization and bioenergy recovery.

The wood pellets subjected to oven-drying at 60 ℃ overnight were pulverized to a desired particle size (120 mesh, particle size < 0.125 mm) for the following homogeneous thermal treatment. An integral process involving high-temperature pyrolysis (800 ℃) combined with steam modification (at 600–800 ℃) was conducted to produce the platform biochar (BC) with both a high oxygen content and a graphitic structure. Specifically, 20 g pulverized wood powders were compacted in a corundum jar. The jar was transferred to a tubular reactor, which was maintained at 200 ℃ under a nitrogen environment (N_2 flow rate of 100 mL min^{-1}) for 2 h to remove residual moisture before the ramping program was initiated. Then, the pyrolytic temperature proceeded to increase with a ramping rate of 5 ℃ min^{-1} to 800 ℃ and maintained for 1 h. A steam tunnel (H_2O flow rate of ~ 5 mL min^{-1}) connected to the tubular reactor was turned on/off, which would induce the water-gas shift and Boudouard reactions at 700–800 ℃. The biochar with minimal RAMs was also fabricated by the same procedure [29].

2.3. Manipulation of RAMs on the Mineral-free Biochar Surface

To exclude potential interference of inherent minerals, the BC was further treated with hydrochloric acid (HCl) to remove the inorganic minerals. Specifically, 10 g biochar sample was dispersed into 1 L diluted HCl (500 mM) for 24 h, and the demineralized biochar was denoted as De-BC. The surface RAMs were then tuned based on a previously reported method [30]. The specific procedure is available in **Text S2**. The obtained oxidized De-BC and reduced De-BC were denoted as OBC and RBC, respectively.

2.4. Introduction of Sulfur Contents

Sulfur contents were introduced into the biochar samples by an annealing treatment. The biochars were sieved into a particle size lower than 0.074 mm. An equivalent amount of precipitate sulfur (S_8) and the biochars were ground for 10 min using an agate mortar and pestle for homogeneous mixing. Subsequently, the mixed powder was transferred into the tubular reactor purged with a N_2 flow (100 mL min^{-1}), and pyrolyzed at 500 or 800 ℃ to manipulate the sulfur speciation. The ramping rate and holding time were set as 5 ℃ min^{-1} and 1 h, respectively. A gas-collecting vessel containing diluted alkaline solution (5 wt.% NaOH) was used to prevent the release of acidic gases (*i.e.*, SO_2 and CO_2) to minimize pollutant discharge. The resultant sulfur-incorporated biochar was denoted as SBCX, where X represented the peak temperature. The OBC and RBC were also used as precursors to prepare SBC following the same procedure as aforementioned, which were designated as SOBCX and SRBCX, respectively.

2.5. Sulfur-doped Biochar Characterization

Detailed information about transmission electron microscopy (TEM, JEOL 2100F, Japan), Raman spectroscopy (Renishaw, UK), X-ray photoelectron spectroscopy (XPS, Thermo Fisher

Scientific, USA), *etc.*, can be found in **Text S3**. The electron paramagnetic resonance (EPR, Bruker, Germany, **Text S4**) analysis was performed with different spin-trapping agents including 5,5-dimethyl-1-pyrrolidine N−Oxide (DMPO) and 2,2,6,6-tetramethyl-4-piperidone (TEMP). Simulation of the sulfur incorporation process was conducted using the thermogravimetric analysis (TG, Rigaku Thermo Plus, USA). Ash contents of all the biochar samples were measured based on a standard method (ASTM D2584, D5630, ISO 3451, **Text S5**). Sulfate and sulfide contents of the biochar were extracted by two different solvents, *i.e.*, diammonium ethylenediaminetetraacetate monohydrate (50 mM) dissolved in DI and diluted HCl (500 mM) [31]. Specifically, each sample (0.5 g) was suspended in a 50 mL respective solvent, and underwent up-to-down rotation overnight. The released SO_4^{2-} ions were detected using an ion chromatography system (Thermo Scientific, USA). The obtained samples were labelled as De-DI SBCX and De-HCl SBCX, respectively. Redox states of the biochar were quantified by the mediated electrochemical reduction and oxidation (MER, MEO) method, which was adopted from the method described in previous papers [32, 33]. Detailed information is available in **Text S6**.

2.6. Activity Evaluation and Analytical Methods

An omnipresent hazardous organic pollutant in water resources, bisphenol A ($C_{15}H_{16}O_2$, BPA), was selected to evaluate the catalytic activity of all biochar samples in batch experiments with PMS as an oxidant [14, 34]. Specifically, a 100 mL solution at an initial concentration of 50 mg L^{-1} (or as otherwise specified) BPA was transferred into a 250 mL conical flask. Then, the biochar (0.3 g L^{-1}) and Oxone powder (1 g L^{-1}, equivalent to 3.25 mM PMS) were promptly added to initiate the reaction. All the selected experimental parameters were determined in preliminary tests, and the experiments were conducted in triplicates within an oscillator under vigorous stirring at 200 rpm, an ambient temperature of 25 ± 1 ℃, and an initial pH of 5.8 ±

0.2 without light irradiation. No buffer agent was involved, as conventional buffers (carbonate, bicarbonate, or phosphorus) may scavenge the radicals or influence the surface properties of carbon [35]. Detailed information about the experimental protocols, analytical parameters for the high-performance liquid chromatography (HPLC), total organic carbon (TOC) as well as inorganic carbon (IC), residual PMS, in-situ Raman Analysis, scavenging experiments, *etc.*, can be found in **Text S7**–**S9**.

3. Results and Discussion

3.1. Biochars with Distinct Minerals and RAMs

SEM images of all the biochar samples showed a similar typical honeycomb porous structure where slit-like channels intercalated with dense micrometer-scale macropores (< 10 μm, **Fig. S1**), probably derived from a continuous vessel system in lignocellulosic biomass. A high surface area (429 m^2 g^{-1}, **Table S1a**) and three-dimensional porous structure of the BC would be conducive to mass transfer in the heteroatom doping and carbocatalysis processes [36]. Calcite (JCPDS card PDF#05-0586, **Fig. S2**) was the main mineral in wood-derived biochar, and the demineralization treatment (by HCl) effectively removed all calcite in the BC (from 9.6 wt.% to below detection limit, based on comparison with the resultant De-BC, OBCs, and RBCs, **Table S2**).

OFGs in the biochar also varied under controlled redox states. The FTIR analysis showed a high density of hydroxyl −OH, ketonic C=O, and incorporated C−O−C groups on the BC (**Fig. 1a**). Zhong, Jiang, Zhao, Wang, Chen, Ren, Liu, Zhang, Tsang and Crittenden [30] reported that the reductive treatment using $NaBH_4$ could transform those recalcitrant OFGs (*i.e.*, ketonic C=O) into oxygenated carbon-centered PFRs ($C{-}O^{\bullet}$), while the H_2O_2 treatment switched back this conversion. The oxidation process (H_2O_2 treatment) transformed much of the hydroxyl −OH into ketonic C=O (OBC), while all the characteristic peaks disappeared after the BC reduction (RBC). The degree of carbonation (C−O/C=O, **Fig. S3** and **S4**) obtained from O 1s XPS spectra also confirmed higher levels of ketonic C=O in the OBCs and higher densities of C−O in the RBCs, which further verified this redox transformation. Moreover, the EPR analysis (**Fig. 1b**) demonstrated that oxygenated carbon-centered PFRs (Landé factor range 2.0030−2.0040) on the BC were transformed into oxygen-centered PFRs (g-factor over 2.0040) on the OBC due to attenuation of C−O$^{\bullet}$ into C=O groups during the H_2O_2 treatment. By contrast, C−O$^{\bullet}$ radicals were formed on the RBC with a g-factor (2.0032−2.0033) resembling that of the BC apart from an increased signal intensity.

3.2. Incorporation of Sulfur into Biochar

Higher sulfur contents (7.6−7.9%, **Table S2**) in the high-temperature annealed SBCs than the BC indicated a successful impregnation of thermal-stable structural sulfur instead of elemental sulfur (boiling point of S_8 at ~ 444 ℃) into biochar. The precipitated sulfur possibly acted as a pore-forming agent (average pore diameter of SBCs expanded from 3.87 to 4.08−5.15 nm, **Table S1a**) and created more discernable porous channels (**Fig. S1**) during the sulfur incorporation, ascribed to its high fluidity after linkage cleavage at 130−160 ℃ [37]. It is noted that those evaporated sulfurs were recovered using a cooling tube, which would effectively reduce the chemical input and pollutant release. Thus, precipitated sulfur was more advantageous than other conventional pore-forming agents (*e.g.*, NH_4Cl and $ZnCl_2$) that would potentially release greenhouse gases or require inconvenient post-treatment to remove deposited salt monolayers.

The structural sulfur formed on biochar might be either mineral sulfur (S^{2-} and SO_4^{2-}) or incorporated sulfur in the carbon lattice. A lower sulfur content (0.8−5.3%) was found in the sulfur biochar (SOBCs and SRBCs) produced from the demineralized biochar (OBC and RBC), suggesting a nonnegligible role of inherent minerals in harboring sulfur. In addition, PFRs might also participate in the sulfur doping, evidenced by a much higher sulfur content in the SRBCs than the SOBCs (1.4−5.3% > 0.8−1.1%, **Table S2**). However, the PFRs-incorporated sulfur contents decreased remarkably (from 5.3% in the SRBC500 to 1.4% in the SRBC800) under a higher temperature.

3.3. High Affinity of Calcite towards Sulfate

A lower surface area (159 and 382 m^2 g^{-1}) and dilated porous structures (11.1−12.2 nm) of the SBCs confirmed that the incorporated sulfur existed mainly in forms of particles/clusters (rather than organosulfur or sulfur heteroatoms) on the BC surface that would marginally impact the biochar surface characteristics [27]. The TG results presented a prominent mass decay in the SBCs over a temperature range of 224–231 ℃ (**Fig. S5**) which is below the theoretical boiling point of sulfur, verifying the reactions occurring between sulfur and inherent biochar minerals. The XRD patterns illustrated that calcite in the BC interacted with sulfur during heating and was converted into CaS (JCPDS card, PDF#08-0464, **Fig. S2** and **R. 1**), consistent with the TG analysis.

$$2\mathrm{CaCO_3} + 2S \rightarrow \mathrm{CaS} + \mathrm{SO_2} + 2\mathrm{CO_2} \qquad \textbf{(R. 1)}$$

Wang, Guo, Liu, Si, Luo, Zhao and Ren [20] suggested that sulfur incorporation into biochar barely impacted its oxygen level. Similar results were also found in this work where the sulfur doping only showed a minor effect on the oxygen contents during annealing (10.3−10.8 *vs* 12.6 wt.%), indicating that the OFGs might not be the primary sites to accommodate sulfur in the presence of minerals. It is commonly acknowledged that sulfur is difficult to be directly incorporated into carbon allotropes (*e.g.*, graphene or CNTs) without mineral impurities [38-40]. Thus, calcite in biochar might have a stronger affinity to coordinate sulfur than OFGs.

3.4. Transformation of Sulfate to Sulfide

Changes in mineral sulfur speciation in the SBCs were quantified by solvent extraction (**Fig. 2a**). The BC contained a negligible amount of sulfate (< 2 mg g^{-1}), which was elevated to 15.3 mg g^{-1} after sulfur doping at a moderate temperature of 500 ℃ (SBC500). The further increase of annealing temperature to 800 ℃ (SBC800) reduced the sulfate amount to 3.2 mg g^{-1}. The characteristic diffraction peak of $CaSO_4$ cannot be retrieved in the XRD patterns of the SBCs, probably due to its non-crystalline feature or interference from the co-existing sulfide (**Fig. S2** and **S3**). The TEM images (**Fig. S6**) presented an accumulation and deposition of amorphous minerals on the peripheries of the SBC500. Comparatively, a discernible fringe lattice of 2.0 Å assigned to the (220) plane of CaS was found on the SBC800. Thus, sulfate was possibly reduced to sulfide by the carbon framework (**R. 2**) during thermal treatment [8].

$$\equiv \mathrm{Biochar} + \mathrm{CaSO_4} \rightarrow \equiv \mathrm{Biochar} + \mathrm{CaS} + \mathrm{CO_2} \qquad (\mathbf{R.\ 2})$$

Based on the sulfur mass balance (**Fig. 2b**), the residual (or non-extractable) sulfur, which was commonly considered as S dopant, accounted for a large fraction of the total sulfur content (2.9%) in the SBC prepared under a moderate annealing temperature of 500 ℃. Intriguingly, the residual sulfur content was as low as 0.4% in the SBC800, contradicting the generally accepted assumption that a higher temperature would favor heteroatom doping [41].

Phase conversion of sulfur minerals in the SBCs was further investigated according to the TG tests of the solvent-extracted SBCs (**Fig. 2c**). Compared with the De-DI SBCs, the differences in mass decay of the pristine and De-HCl SBC500 (or De-HCl SBC800) were calculated as 8.2% (or 0.8%) and 3.5% (or 4.1%), corresponding to the sulfate and sulfide content in the SBCs (**Fig. 2b**), respectively. The derivative TG (DTG) curves suggested that sulfur minerals (especially sulfide) in the SBCs possessed a high thermal stability. Decomposition of $CaSO_4$ occurred at 733 ℃ in the SBC500, which was slightly shifted to a higher temperature (741 ℃) in the De-DI SBC500, attributed to the larger fraction of CaS. A similar shifting trend from 840 to 932 ℃ was also observed for the SBC800. Although the De-HCl SBC500 possessed a sulfur level of ~ 2.8%, it showed an inferior catalytic performance in the preliminary experiment. It was speculated that the residual sulfur content was still in an inert form (*i.e.*, sulfate), and the extraction procedure could not completely remove all the inorganic sulfur when tightly bound to minerals, especially for those trapped in deeper channels. Hence, a pre-demineralization procedure to avoid interaction between inherent biochar minerals and sulfur was indispensable for a valid evaluation of the sulfur doping technique and its effect on carbocatalysis.

3.5. Sulfur Doping into Carbon Framework after Demineralization

A discernible C−S bond (FTIR peak at 710 cm^{-1}) and C−SR bond (5−45 ppm in the ^{13}C NMR spectrum) were only observed in the SRBC500 **(Fig. 3a)**, suggesting a successful doping of sulfur into its carbon framework in the absence of minerals. No characteristic peak (at 40−60 ppm) of sulfoxide/sulfone was found for all the samples, further corroborating that OFGs were not involved in sulfur incorporation. With an increase in the annealing temperature of the RBC and OBC from 500 to 800 ℃, the peak center of the sp^2 hybridization carbon slightly shifted to a higher position (100−150 ppm) while that of the ketonic C=O group remained unchanged. The ultimate analysis (**Table S1b**) and elemental composition from the XPS results (**Table S3**) demonstrated a higher sulfur level in the SRBCs than the SOBCs, indicating that the ketonic C=O group was not the primary site to accommodate sulfur. The sulfurized carbon units with a lattice fringe of 0.31 nm were present in the SRBC500 (**Fig. 1c**), close to that observed in sulfur-doped carbon dots [42]. The SRBC800 only consisted of stacked graphite layers with a lattice fringe of 0.21 nm (**Fig. 1d**), which might correspond to the vulnerability of sulfur dopants towards a temperature higher than 500 ℃. A similar thermal instability of nitrogen dopants was also revealed in our recent work [18].

3.6. Formation of C−S−O *via* Phenoxyl PFRs

The roles of PFRs were investigated by EPR analysis of the unpaired paramagnetic electrons (**Fig. 1b**). The C−O$^\bullet$ radical (g-factor of 2.0032−2.0033) was detected in both the RBC and SRBC500; however, the signal intensity declined in the SRBC500, possibly due to PFRs consumption after the sulfur introduction. In contrast, introducing nitrogen dopants into biochar matrices mediates the intramolecular electron rearrangement, favoring the generation of carbon-centered PFRs with enhanced EPR signals [15]. The distinct phenomenon for sulfur doping suggested that the doped sulfur atoms might interact with phenoxyl-type PFRs to form an integral structure, rather than to merely abstract electrons/protons and evolve carbon-centered PFRs. The deconvoluted XPS spectra of the S 2p binding states (**Fig. 3b** and **S7**) showed a high density (32.4%) of the $-C-SO_x-$ bonding (168.7 eV) in the SRBC500, while only thiophene S (C−S−C $2p_{3/2}$ and $2p_{1/2}$ at 163.2 and 164.5 eV [43], respectively) was found in the other SRBCs and SOBCs. The C=C double bond in the RBC was drastically transformed into C−C in the SRBC500 (C−C/C=C ratio of 41.8, **Fig. S8**). It was speculated therefore that the doped sulfur atoms existed mainly in the form of a C−S−O configuration (**Fig. S9**).

3.7. Contribution of Vacancies Defects for C−S−O Formation

The defective structures of SBCs were studied to explore the formation mechanism of C−S−O combined structure. In principle, the doping of heteroatoms commonly affects the defect level of carbons. It was proposed that the incorporation of sulfur atoms preferred to substitute the carbon atoms at zigzag edges for a lower formation energy [44]. Raman spectroscopy provides a valuable technique to confirm this sulfur doping mechanism by unveiling the change of hybridization structures.

All Raman spectra were deconvoluted into five characteristic peaks (**Fig. 3c** and **S10**), *i.e.*, S band, D band, V band, G1 band, and G2 band at 1230, 1332, 1420, 1522, and 1595 cm^{-1}, respectively [18, 45]. The conventional D band corresponds to A_{1g} symmetry vibration mode of defects or disorder arrangement of carbon atoms. The G band, assigned to E_{2g} symmetry vibration mode of sp^2 hybridization carbon atoms, were divided into G1 band (short-chain aromatics with 3−5 rings) and G2 band (highly ordered sp^2 hybridized aromatics) [46]. To obtain more information about hybridization changes, S band and V band were also introduced, indicating the sp^2/sp^3 hybridization transformation and the deterioration of crystallinity into an amorphous phase [47], respectively.

The oxidative treatment of the BC decreased its defect level (A_D/A_{G1} ratio from 0.55 to 0.43, **Table S4**) possibly due to the newly formed ketonic C=O groups, contrary to an increased ratio to 0.70 in the RBC subjected to the reduction treatment [48]. This phenomenon suggested that the reduction process could lower the density of OFGs that did not favor sulfur doping whilst exposing more defects. The A_D/A_{G1} values of the SOBCs and SRBC800 either increased or remained unchanged due to a pore forming effect of sulfur (**Table S1b**). In contrast, the A_D/A_{G1} value of the SRBC500 dropped sharply to 0.21, confirming the consumption of defects as sulfur doping sites. The ratio of A_{G1}/A_{G2} as a graphitization indicator did not change obviously between the SOBCs and SRBCs, indicating a low contribution from graphitic structures to sulfur doping.

The A_D/A_V ratio can help to categorize the type of dominant defects, where defect transforms sequentially from edges to vacancies following the increase of A_D/A_V [49]. The A_D/A_V values of SOBCs elevated to higher values, suggesting that more vacancies were generated during pore forming and functionality decomposition. However, the decrease in A_D/A_V of SRBC500 from 1.20 to 0.27 indicated that the vacancies were consumed during sulfur doping. Those occupied vacancies could be released after the decomposition of sulfur heteroatoms at 800 ℃ (A_D/A_V of SRBC800, 1.61). The above results validated a predominant contribution from the vacancies to sulfur doping.

3.8. Enhanced Electron-accepting Capacity

Defects and hybridization structures closely correlate with the electronic properties of carbon materials [7]. The sulfur doping process barely impacted electron-donating capacity (EDC) of the biochar irrespective of the small spikes (0.28−0.30 mmol e^- g^{-1} biochar) derived from oxygen introduction and PFRs generation (**Fig. 3d** and **S11**). The SRBC500 showed a comparable electron-accepting capacity (EAC, 0.90 mmol e^- g^{-1} biochar) to that of the OBC (0.87 mmol e^- g^{-1} biochar), which possessed rich electron-withdrawing ketonic groups. This result signified the electrophilic nature of the C−S−O combined structure. After diminishing the sulfur content under a higher temperature, the EAC of the SRBC800 was approximately that of the SOBC800 (0.48 and 0.58 mmol e^- g^{-1} biochar, respectively).

The addition of PMS molecules to ketonic groups is considered as the most critical step (**R. 3**) during a typical nucleophilic PMS activation, *i.e.*, singlet oxygenation [50]. Given that the C−S−O combined structure maintained a similar electrophilic state with that of ketonic groups, a mild and sustainable PMS activation could be therefore expected. Hence, the SRBC500 with the highest EAC was selected as a representative sulfur-doped biochar to further investigate its catalytic mechanisms.

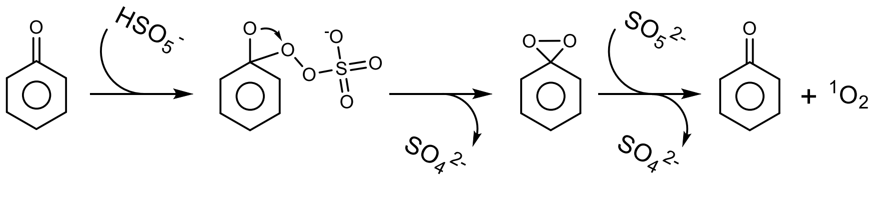

(R. 3)

3.9. High Catalytic Performance of the Doped Sulfur

Catalytic activities of the SBCs were evaluated in terms of their performance in BPA degradation. The obtained kinetic data were fitted using a pseudo-first-order model. PMS alone showed almost no reactivity to degrade BPA (~ 3% in 90 min, **Fig. 4a**). All the undoped biochar and sulfur-doped biochar with similar textural characteristics (**Table S3**) presented limited and similar BPA adsorption capacities (25.1−35.9% in 90 min, **Fig. 4b**), which excluded the impact of diffusion or mass transfer on catalytic degradation.

It should be noted that the SBCs with rich inorganic sulfur minerals (SBC500 and SBC800) failed to activate PMS for BPA degradation (k_{obs} = 0.0089−0.0111 min^{-1}, **Fig. S12**). The BPA removal rate markedly increased (to ~ 50% and 66.3%) in the presence of the OBC with enriched OFGs, and RBC with abundant electron-donating PFRs, respectively. Intriguingly, the SRBC500 exhibited a superior removal rate of over 90%, suggesting a promoted peroxide activation by the doped sulfur atoms. Hence, the inert mineral contents can be potentially mistaken as doped sulfur contents leading to an underestimation of sulfur dopants in carbocatalysis. A further increase in pyrolysis temperature to 800 °C induced the decomposition of the C−S−O combined structure and thus resulted in an inhibited BPA degradation (71.2%, **Fig. 4b**), reaffirming the critical role of sulfur dopants.

After PMS addition, only the SRBC500 showed a significantly improved TOC removal (82.5% *vs* 40.7%, **Fig. S13**), corroborating its high mineralization performance in water disinfection. In contrast, PMS introduction caused either trivial or adverse effects on TOC removal by the other biochars. The above data collectively confirmed that BC, RBC, and RSBC800 had no or limited mineralization ability as their TOC removals were highly dependent on adsorption, and might undergo a strong oxidation of active sites on the biochar surface after contacting reactive oxygen species (ROS). This phenomenon indicated the superiority of sulfur heteroatoms doped into the carbon framework for inducing the formation of mild ROS, which could preserve the carbocatalysis of biochar to reach a durable water remediation.

3.10. Catalytic Mechanisms of Sulfur Heteroatoms

Various scavengers (*i.e.*, ethanol (EtOH), *tert*-butyl alcohol (TBA), and sodium azide (NaN_3)) were applied to identify the ROS involved (*i.e.*, $^\bullet OH$, $^\bullet SO_4^-$, and $^1O_2$) in the catalytic behavior of SRBC500 (**Table S5** and **Fig. S14a**). All the ROS in the bulk solution can be quenched by NaN_3, while TBA and EtOH selectively target for $^{\bullet}OH$ and $^{\bullet}OH/^{\bullet}SO_4^-$ (**Text S10**), respectively.

A relatively minor decrease of BPA removal (from 91.1% to 73.4−76.9%, **Fig. 5a**) by the SRBC500 with the addition of EtOH or NaN_3 implied that $^{\bullet}OH$ and $^{\bullet}SO_4^-$ were not the primary ROS responsible for BPA degradation. Intriguingly, the addition of TBA dramatically reduced the degradation efficiency to 38.5%, with the corresponding rate constant (k_{obs}) dropping by 83.9%. These contradictory observations might be due to the hydrophobic compound (*i.e.*, TBA) obstructing the contact between peroxide molecules and surface active sites [51]. Therefore, the formation of reactive species was probably initiated by an interfacial interaction between PMS and the C−S−O combined structure.

EPR analysis was employed to shed light on the ROS generated during the catalytic reaction. No signal was detected in the absence of catalysts with DMPO as the radical trapping agent (**Fig. 5b**). Clear characteristic peaks assigned to the DMPO−OH ($\alpha H = \alpha N = 14.9$ G) were found in all the biochars, while weak peaks corresponding to the DMPO−SO_4 ($\alpha N = 13.5$ G, $\alpha H = 9.9$ G, $\alpha_{\gamma 1}H = 1.3$ G, and $\alpha_{\gamma 2}H = 0.9$) were only detected in the BC and RBC. The OFGs and PFRs would directly donate electrons to activate PMS, and the adsorbed water on the biochar surface could be promptly oxidized to generate $^{\bullet}OH$ [16, 52]. A lower signal intensity of the SRBC500 suggested that the catalytic reactivity of sulfur dopants did not rely on radicals present in bulk solution, which was consistent with the results of the scavenging experiments.

Another trapping agent, TEMP, which is susceptible to $^1O_2$, was also employed (**Fig. 5c**) to further probe the surface redox process. Sharp triplet peaks ($\alpha N = 16.3$ G) resulting from the reaction between TEMP and $^1O_2$ were found in the SRBC500. The peak intensity of the SRBC500 was 3.3- and 5.3-fold higher than that of the BC and RBC, respectively. These results confirmed that $^1O_2$ was the primary ROS, which mainly originated from interfacial reactions on the SRBC500 surface.

3.11. Electroactive Affinity towards Nucleophiles

To attain the rate-determining factor of the catalytic reaction, a series of catalyst loadings, PDS dosages, and BPA concentrations were employed in batch experiments, and their corresponding k_{obs} values were calculated. An increase in catalyst and PMS dosages elevated the k_{obs} (**Fig. S14b** and **S14c**), while a higher BPA concentration delayed the reaction rate (**Fig. S14d**). The logarithms of k_{obs} showed strong linearity with these varied experimental parameters ($R^2 = 0.86–0.96$, **Fig. 5d**). The slopes of $\ln(k_{obs})$ against $\ln([\text{Catalyst}]_0)$, $\ln([\text{BPA}]_0)$, and $\ln([\text{PMS}]_0)$, representing the orders of each integral reaction, were 0.95, -0.62, and 0.65, respectively. The similar reaction orders of BPA concentration and PMS dosage possibly indicated a high affinity of the C−S−O configuration towards PMS, which was comparable to the rate of BPA adsorption *via* π-π interaction [53]. The reaction order of PMS dosage reported in this study (0.65) was much higher than those reported in the literature (< 0.1) where PMS was anchored by limited active sites in typical non-radical reactions [8]. Thus, the preponderance of the proposed sulfur heteroatom doping technique lies in an atomical dispersion of active sites over carbon units with little steric hindrance, which enabled a stoichiometric aqueous carbocatalysis to avoid pollutant deposition.

3.12. Electroactive Affinity towards Nucleophiles

The affinity of biochars towards PMS was probed *via* measuring their PMS adsorption capacities at initial (5 min) and equilibrium (30 min) stages, respectively. The SRBC500 exhibited a high initial PMS adsorptive capacity comparable to that of the OBC with rich ketonic C=O groups (1.09 *vs* 1.04 mM g^{-1}, **Fig. 6a**), which implied a strong affinity to attract PMS due to its electrophilic nature [50]. The difference between the values at different times could reflect the durability of the doped sulfur atoms to endure passivation (SRBC500, 0.99 mM g^{-1}). After diminishing the C−S−O structure under an annealing temperature of 800 °C, the SRBC800 showed an inferior durability in PMS adsorption (0.74−0.79 mmol g^{-1}) close to that of the BC (0.70−0.82 mmol g^{-1}). The above results were in alignment with the BPA and TOC removal results, indicating the electron-withdrawing C−S−O bonding was mainly responsible for the carbocatalysis.

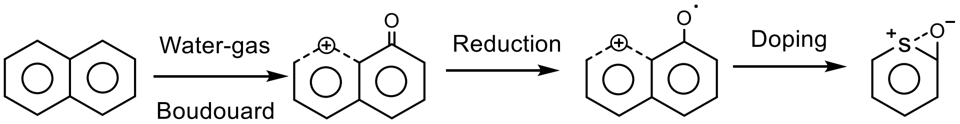

(R. 4)

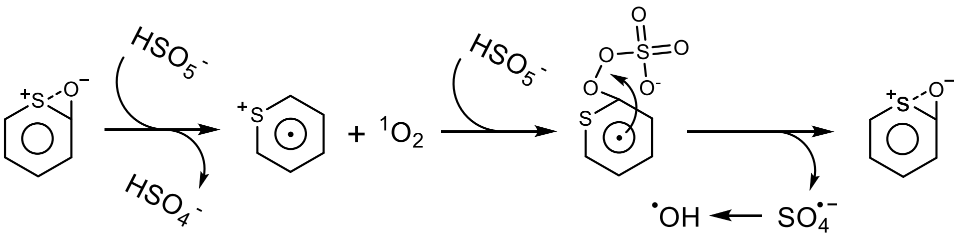

(R. 5)

3.13. Formation Mechanisms of Interfacial $^1O_2$

The *in-situ* Raman spectra were scrutinized to explore the $^1O_2$ generation pathway (**Fig. 6b**). Three characteristic peaks at approximately 831, 885 or 1072, and 973 cm^{-1} correspond to the metastable surface-confined complex ($*HSO_5^-$), PMS molecules (HSO_5^-), and sulfate ions (HSO_4^-), respectively. An evolved peak of $*HSO_5^-$, a critical intermediate during $^1O_2$ formation, with a low intensity was found in the SRBC500. Due to a similar electronegativity of carbon and sulfur atoms ($\chi_C = 2.55$, $\chi_S = 2.58$), sulfur atoms that occupied the vacancies interacted with adjacent phenoxyl-type PFRs to form an epoxide-like structure during the sulfur doping process (**R. 4**). The epoxide-like C−S−O could act as an electrophile similar to dioxirane (**R. 3**) to induce a nucleophilic addition of PMS with the generation of $^1O_2$ and aryl radical [54, 55]. The metastable $*HSO_5^-$ was formed as an intermediate after the nucleophilic addition of another PMS molecule upon aryl radical, and subsequently mediated recovery of the epoxide-like C−S−O bonding with $SO_4^{\bullet-}$ radicals generated as the by-product (**R. 5**).

During the ROS transformation, a small amount of adsorbed water was oxidized into $^{\bullet}OH$. Compared with the ketone-induced $^1O_2$ formation, this process started from the generation of interfacial $^1O_2$ without releasing it into bulk solution, accounting for the higher durability and faster kinetics of sulfur-doped biochar. This catalytic pathway is basically an interfacial reaction with less ROS dissipated and thus promises a sustainable stoichiometry in aqueous decontamination.

4. Conclusions

Few studies to date have addressed the critical implications of inherent biochar components during heteroatom doping. Neither the doping mechanisms nor the structure-performance relationships for heteroatoms have been scrutinized *via* a component-specific methodology. This has been the major knowledge gap impeding, or even misleading sometimes, the hypothesis-driven development of heteroatom-doped biochar in the field of environmental technology. In order to tackle this current limitation, we studied separately the impacts of two inherent components (*i.e.*, minerals and RAMs) of biochar on the process of sulfur doping. Our results revealed that the endogenous calcite interfered with the sulfur doping by forming inactive sulfur minerals (*i.e.*, $CaSO_4$ and CaS). Comparatively, the vacancies and phenoxyl-type PFRs played a vital role in accommodating sulfur atoms to configure an epoxide-like C−S−O structure with a high affinity towards PMS, and then induced a nucleophilic addition that triggered the generation of $^1O_2$ and $^{\bullet}OH$ for an efficient abatement of BPA. New scientific understanding offered in this study can potentially be applied to biochars derived from other biomass wastes and heteroatoms, helping to stimulate innovative synthesis and extensive utilization of ingenious heteroatom-doped biochar. Overall, our study advances the scientific design of high-efficacy heteroatom-doped biochar for actualizing sustainable waste management and green water remediation.

Declaration of competing interest

The authors declare that they have no known competing financial interests or personal relationships that could influence the work reported.

Acknowledgement

The authors appreciate the financial support from the Hong Kong Research Grants Council (PolyU 15222020) and Hong Kong Green Tech Fund (GTF202020153). The support from the University Research Facility on Chemical and Environmental Analysis (UCEA) of PolyU is also gratefully acknowledged.

Supporting Information

This provides the following: detailed procedures of the characterizations employed (SEM, TEM, Raman, XPS, EPR, *etc*.) and electrochemical tests (EDC/EAC); kinetics curves of the organic degradation and the PMS adsorption; supplementary tables and Fig.s for the material morphology, elemental compositions, structural information, and catalysis.

REFERENCES

[1] M.M. Mekonnen, A.Y. Hoekstra, Four billion people facing severe water scarcity, Sci. Adv., 2 (2016) e1500323.

[2] A.U. Rajapaksha, S.S. Chen, D.C.W. Tsang, M. Zhang, M. Vithanage, S. Mandal, B. Gao, N.S. Bolan, Y.S. Ok, Engineered/designer biochar for contaminant removal/immobilization from soil and water: Potential and implication of biochar modification, Chemosphere, 148 (2016) 276-291.

[3] A.D. Igalavithana, S. Mandal, N.K. Niazi, M. Vithanage, S.J. Parikh, F.N.D. Mukome,

M. Rizwan, P. Oleszczuk, M. Al-Wabel, N. Bolan, D.C.W. Tsang, K.-H. Kim, Y.S. Ok, Advances and future directions of biochar characterization methods and applications, Crit. Rev. Env. Sci. Technol., 47 (2017) 2275-2330.

[4] W.-J. Liu, H. Jiang, H.-Q. Yu, Emerging applications of biochar-based materials for energy storage and conversion, Energ. Environ. Sci., 12 (2019) 1751-1779.

[5] Z. Wan, Y. Sun, D.C.W. Tsang, E. Khan, A.C.K. Yip, Y.H. Ng, J. Rinklebe, Y.S. Ok, Customised fabrication of nitrogen-doped biochar for environmental and energy applications, Chem. Eng. J., 401 (2020) 126136.

[6] X. Duan, H. Sun, S. Wang, Metal-free carbocatalysis in advanced oxidation reactions, Acc. Chem. Res., 51 (2018) 678.

[7] Z. Wan, Y. Sun, D.C.W. Tsang, D. Hou, X. Cao, S. Zhang, B. Gao, Y.S. Ok, Sustainable remediation with electroactive biochar system: Mechanisms and perspectives, Green Chem., 22 (2020) 2688-2711.

[8] Z. Wan, Y. Sun, D.C.W. Tsang, I.K.M. Yu, J. Fan, J.H. Clark, Y. Zhou, X. Cao, B. Gao, Y.S. Ok, A sustainable biochar catalyst synergized with copper heteroatoms and CO_2 for singlet oxygenation and electron transfer routes, Green Chem., 21 (2019) 4800-4814.

[9] W.-J. Liu, H. Jiang, H.-Q. Yu, Development of Biochar-Based Functional Materials: Toward a Sustainable Platform Carbon Material, Chem. Rev., 115 (2015) 12251-12285.

[10] W.-D. Oh, T.-T. Lim, Design and application of heterogeneous catalysts as peroxydisulfate activator for organics removal: An overview, Chem. Eng. J., 358 (2019) 110-133.

[11] W. Zhang, Y. Li, X. Fan, F. Zhang, G. Zhang, Y.-A. Zhu, W. Peng, S. Wang, X. Duan, Synergy of nitrogen doping and structural defects on hierarchically porous carbons toward catalytic oxidation via a non-radical pathway, Carbon, 155 (2019) 268-278.

[12] L.-L. Ling, W.-J. Liu, S. Zhang, H. Jiang, Magnesium Oxide Embedded Nitrogen Self-

Doped Biochar Composites: Fast and High-Efficiency Adsorption of Heavy Metals in an Aqueous Solution, Environ. Sci. Technol., 51 (2017) 10081-10089.

[13] S. Zhu, C. Jin, X. Duan, S. Wang, S.-H. Ho, Nonradical oxidation in persulfate activation by graphene-like nanosheets (GNS): Differentiating the contributions of singlet oxygen (1O2) and sorption-dependent electron transfer, Chem. Eng. J., 393 (2020) 124725.

[14] Z. Wan, Y. Sun, D.C.W. Tsang, Z. Xu, E. Khan, S.-H. Liu, X. Cao, Sustainable impact of tartaric acid as electron shuttle on hierarchical iron-incorporated biochar, Chem. Eng. J., 395 (2020) 125138.

[15] S. Zhu, X. Huang, X. Yang, P. Peng, Z. Li, C. Jin, Enhanced transformation of Cr(VI) by heterocyclic-N within nitrogen-doped biochar: Impact of surface modulatory persistent free radicals (PFRs), Environ. Sci. Technol., 54 (2020) 8123-8132.

[16] S. Zhu, X. Huang, F. Ma, L. Wang, X. Duan, S. Wang, Catalytic removal of aqueous contaminants on N-doped graphitic biochars: Inherent roles of adsorption and nonradical mechanisms, Environ. Sci. Technol., 52 (2018) 8649-8658.

[17] S.-H. Ho, Y.-d. Chen, R. Li, C. Zhang, Y. Ge, G. Cao, M. Ma, X. Duan, S. Wang, N.-q. Ren, N-doped graphitic biochars from C-phycocyanin extracted Spirulina residue for catalytic persulfate activation toward nonradical disinfection and organic oxidation, Water Res., 159 (2019) 77-86.

[18] Z. Wan, Z. Xu, Y. Sun, M. He, D. Hou, X. Cao, D.C.W. Tsang, Critical Impact of Nitrogen Vacancies in Nonradical Carbocatalysis on Nitrogen-Doped Graphitic Biochar, Environ. Sci. Technol., 55 (2021) 7004-7014.

[19] W. Kiciński, M. Szala, M. Bystrzejewski, Sulfur-doped porous carbons: Synthesis and applications, Carbon, 68 (2014) 1-32.

[20] H. Wang, W. Guo, B. Liu, Q. Si, H. Luo, Q. Zhao, N. Ren, Sludge-derived biochar as efficient persulfate activators: Sulfurization-induced electronic structure modulation and

disparate nonradical mechanisms, Appl. Catal. B: Environ., 279 (2020) 119361.

[21] D. Ding, S. Yang, X. Qian, L. Chen, T. Cai, Nitrogen-doping positively whilst sulfur-doping negatively affect the catalytic activity of biochar for the degradation of organic contaminant, Appl. Catal. B: Environ., 263 (2020) 118348.

[22] Y.-d. Chen, R. Wang, X. Duan, S. Wang, N.-q. Ren, S.-H. Ho, Production, properties, and catalytic applications of sludge derived biochar for environmental remediation, Water Res., 187 (2020) 116390.

[23] X. Ruan, Y. Sun, W. Du, Y. Tang, Q. Liu, Z. Zhang, W. Doherty, R.L. Frost, G. Qian, D.C.W. Tsang, Formation, characteristics, and applications of environmentally persistent free radicals in biochars: A review, Bioresour. Technol., 281 (2019) 457-468.

[24] X. Ruan, Y. Liu, G. Wang, R.L. Frost, G. Qian, D.C.W. Tsang, Transformation of functional groups and environmentally persistent free radicals in hydrothermal carbonisation of lignin, Bioresour. Technol., 270 (2018) 223-229.

[25] B. Zhao, D. O'Connor, J. Zhang, T. Peng, Z. Shen, D.C.W. Tsang, D. Hou, Effect of pyrolysis temperature, heating rate, and residence time on rapeseed stem derived biochar, J. Clean. Prod., 174 (2018) 977-987.

[26] H. Nan, F. Yang, L. Zhao, O. Mašek, X. Cao, Z. Xiao, Interaction of Inherent Minerals with Carbon during Biomass Pyrolysis Weakens Biochar Carbon Sequestration Potential, ACS Sustain. Chem. Eng., 7 (2019) 1591-1599.

[27] S. Cheah, S.C. Malone, C.J. Feik, Speciation of Sulfur in Biochar Produced from Pyrolysis and Gasification of Oak and Corn Stover, Environ. Sci. Technol., 48 (2014) 8474-8480.

[28] D. Xu, L. Yang, M. Zhao, J. Zhang, S.S.A. Syed-Hassan, H. Sun, X. Hu, H. Zhang, S. Zhang, Conversion and transformation of N species during pyrolysis of wood-based panels: A review, Environ. Pollut., 270 (2021) 116120.

[29] G. Fang, C. Liu, J. Gao, D.D. Dionysiou, D. Zhou, Manipulation of Persistent Free Radicals in Biochar To Activate Persulfate for Contaminant Degradation, Environ. Sci. Technol., 49 (2015) 5645-5653.

[30] D. Zhong, Y. Jiang, Z. Zhao, L. Wang, J. Chen, S. Ren, Z. Liu, Y. Zhang, D.C.W. Tsang, J.C. Crittenden, pH dependence of arsenic oxidation by rice-husk-derived biochar: Roles of redox-active moieties, Environ. Sci. Technol., 53 (2019) 9034-9044.

[31] B. Zhao, H. Xu, T. Zhang, X. Nan, F. Ma, Effect of pyrolysis temperature on sulfur content, extractable fraction and release of sulfate in corn straw biochar, RSC Adv., 8 (2018) 35611-35617.

[32] Y. Zhang, X. Xu, L. Cao, Y.S. Ok, X. Cao, Characterization and quantification of electron donating capacity and its structure dependence in biochar derived from three waste biomasses, Chemosphere, 211 (2018) 1073-1081.

[33] Y. Zhang, X. Xu, P. Zhang, Z. Ling, H. Qiu, X. Cao, Pyrolysis-temperature depended quinone and carbonyl groups as the electron accepting sites in barley grass derived biochar, Chemosphere, 232 (2019) 273-280.

[34] W.-D. Oh, G. Lisak, R.D. Webster, Y.-N. Liang, A. Veksha, A. Giannis, J.G.S. Moo, J.-W. Lim, T.-T. Lim, Insights into the thermolytic transformation of lignocellulosic biomass waste to redox-active carbocatalyst: Durability of surface active sites, Appl. Catal. B: Environ., 233 (2018) 120-129.

[35] F. Chen, L.-L. Liu, J.-J. Chen, W.-W. Li, Y.-P. Chen, Y.-J. Zhang, J.-H. Wu, S.-C. Mei, Q. Yang, H.-Q. Yu, Efficient decontamination of organic pollutants under high salinity conditions by a nonradical peroxymonosulfate activation system, Water Res., 191 (2021) 116799.

[36] X. Wang, Y. Liu, L. Zhu, Y. Li, K. Wang, K. Qiu, N. Tippayawong, P. Aggarangsi, P. Reubroycharoen, S. Wang, Biomass derived N-doped biochar as efficient catalyst supports for

CO2 methanation, J. CO2 Util., 34 (2019) 733-741.

[37] B. Zhang, H. Gao, P. Yan, S. Petcher, T. Hasell, Inverse vulcanization below the melting point of sulfur, Materials Chemistry Frontiers, 4 (2020) 669-675.

[38] X. Duan, K. O'Donnell, H. Sun, Y. Wang, S. Wang, Sulfur and nitrogen co-doped graphene for metal-free catalytic oxidation reactions, Small, 11 (2015) 3036-3044.

[39] W. Ma, N. Wang, Y. Du, P. Xu, B. Sun, L. Zhang, K.-Y.A. Lin, Human-Hair-Derived N, S-Doped Porous Carbon: An Enrichment and Degradation System for Wastewater Remediation in the Presence of Peroxymonosulfate, ACS Sustain. Chem. Eng., 7 (2019) 2718-2727.

[40] R. Guo, L. Yan, P. Rao, R. Wang, X. Guo, Nitrogen and sulfur co-doped biochar derived from peanut shell with enhanced adsorption capacity for diethyl phthalate, Environ. Pollut., 258 (2020) 113674.

[41] K. Huang, S.-H. Chai, R.T. Mayes, G.M. Veith, K.L. Browning, M.A. Sakwa-Novak, M.E. Potter, C.W. Jones, Y.-T. Wu, S. Dai, An efficient low-temperature route to nitrogen-doping and activation of mesoporous carbons for CO2 capture, Chem. Comm., 51 (2015) 17261-17264.

[42] H. Ding, J.-S. Wei, H.-M. Xiong, Nitrogen and sulfur co-doped carbon dots with strong blue luminescence, Nanoscale, 6 (2014) 13817-13823.

[43] Y. Yan, Y.-X. Yin, S. Xin, Y.-G. Guo, L.-J. Wan, Ionothermal synthesis of sulfur-doped porous carbons hybridized with graphene as superior anode materials for lithium-ion batteries, Chem. Comm., 48 (2012) 10663-10665.

[44] L. Zhang, J. Niu, M. Li, Z. Xia, Catalytic Mechanisms of Sulfur-Doped Graphene as Efficient Oxygen Reduction Reaction Catalysts for Fuel Cells, J. Phys. Chem. C, 118 (2014) 3545-3553.

[45] X. Yang, A.D. Igalavithana, S.E. Oh, H. Nam, M. Zhang, C.H. Wang, E.E. Kwon,

D.C.W. Tsang, Y.S. Ok, Characterization of bioenergy biochar and its utilization for metal/metalloid immobilization in contaminated soil, Sci. Total Environ., 640-641 (2018) 704-713.

[46] L.A. Pérez, N. Bajales, G.I. Lacconi, Raman spectroscopy coupled with AFM scan head: A versatile combination for tailoring graphene oxide/reduced graphene oxide hybrid materials, Appl. Surf. Sci., 495 (2019) 143539.

[47] Q. Yang, Y. Chen, X. Duan, S. Zhou, Y. Niu, H. Sun, L. Zhi, S. Wang, Unzipping carbon nanotubes to nanoribbons for revealing the mechanism of nonradical oxidation by carbocatalysis, Appl. Catal. B: Environ., 276 (2020) 119146.

[48] Q. Yang, Z. Xiao, D. Kong, T. Zhang, X. Duan, S. Zhou, Y. Niu, Y. Shen, H. Sun, S. Wang, L. Zhi, New insight to the role of edges and heteroatoms in nanocarbons for oxygen reduction reaction, Nano Energy, 66 (2019) 104096.

[49] A. Eckmann, A. Felten, A. Mishchenko, L. Britnell, R. Krupke, K.S. Novoselov, C. Casiraghi, Probing the nature of defects in graphene by Raman spectroscopy, Nano Lett., 12 (2012) 3925-3930.

[50] J. Lee, U. von Gunten, J.-H. Kim, Persulfate-based advanced oxidation: Critical assessment of opportunities and roadblocks, Environ. Sci. Technol., 54 (2020) 3064-3081.

[51] S. Cai, Q. Zhang, Z. Wang, S. Hua, D. Ding, T. Cai, R. Zhang, Pyrrolic N-rich biochar without exogenous nitrogen doping as a functional material for bisphenol A removal: Performance and mechanism, Appl. Catal. B: Environ., 291 (2021) 120093.

[52] J. He, Y. Xiao, J. Tang, H. Chen, H. Sun, Persulfate activation with sawdust biochar in aqueous solution by enhanced electron donor-transfer effect, Sci. Total Environ., 690 (2019) 768-777.

[53] M. Teixidó, J.J. Pignatello, J.L. Beltrán, M. Granados, J. Peccia, Speciation of the Ionizable Antibiotic Sulfamethazine on Black Carbon (Biochar), Environ. Sci. Technol., 45

(2011) 10020-10027.

[54] Y. Zhou, J. Jiang, Y. Gao, J. Ma, S.-Y. Pang, J. Li, X.-T. Lu, L.-P. Yuan, Activation of Peroxymonosulfate by Benzoquinone: A Novel Nonradical Oxidation Process, Environ. Sci. Technol., 49 (2015) 12941-12950.

[55] A. Lange, H.-D. Brauer, On the formation of dioxiranes and of singlet oxygen by the ketone-catalysed decomposition of Caro's acid, J. Chem. Soc., Perkin Trans. 2, (1996) 805-811.

List of Figures

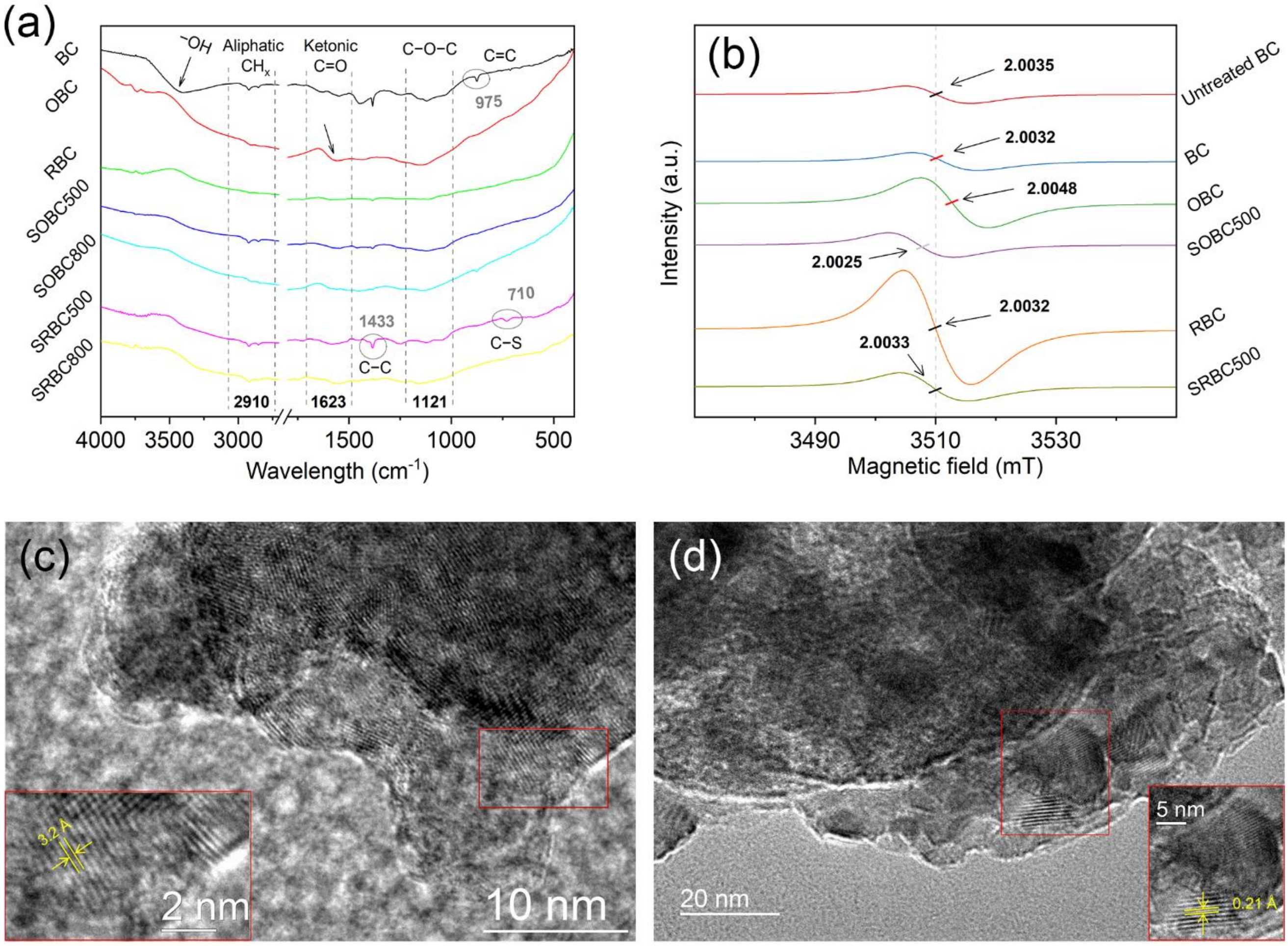

Fig. 1 FTIR (a) and EPR spectra (b) of the selected biochar; and TEM images of the SRBC500 (c) and SRBC800 (d).

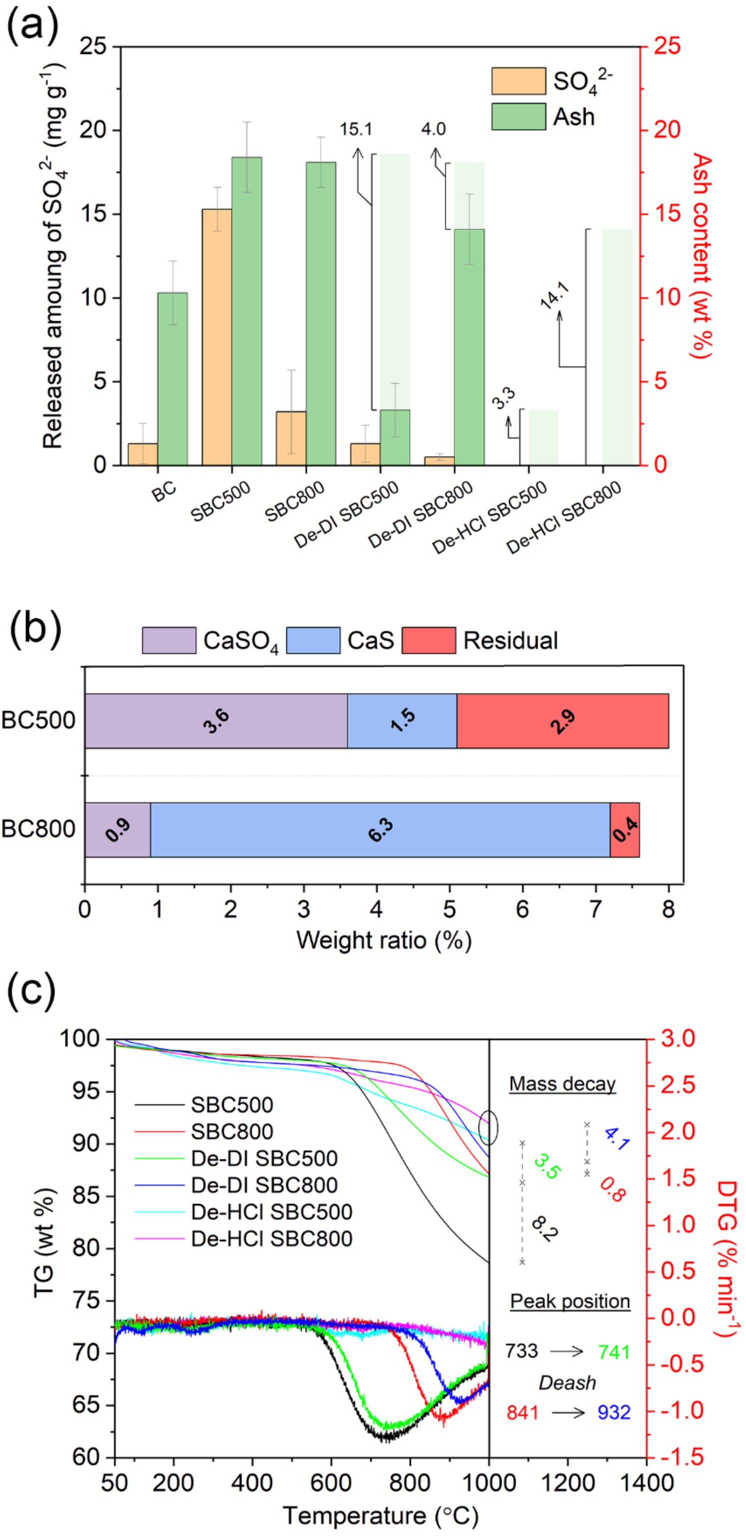

Fig. 2 Amount of released SO_4^{2-} and mineral content in biochar (a); sulfur distribution of the SBCs (b); and TG-DTG analysis of the pristine and demineralized SBCs (c).

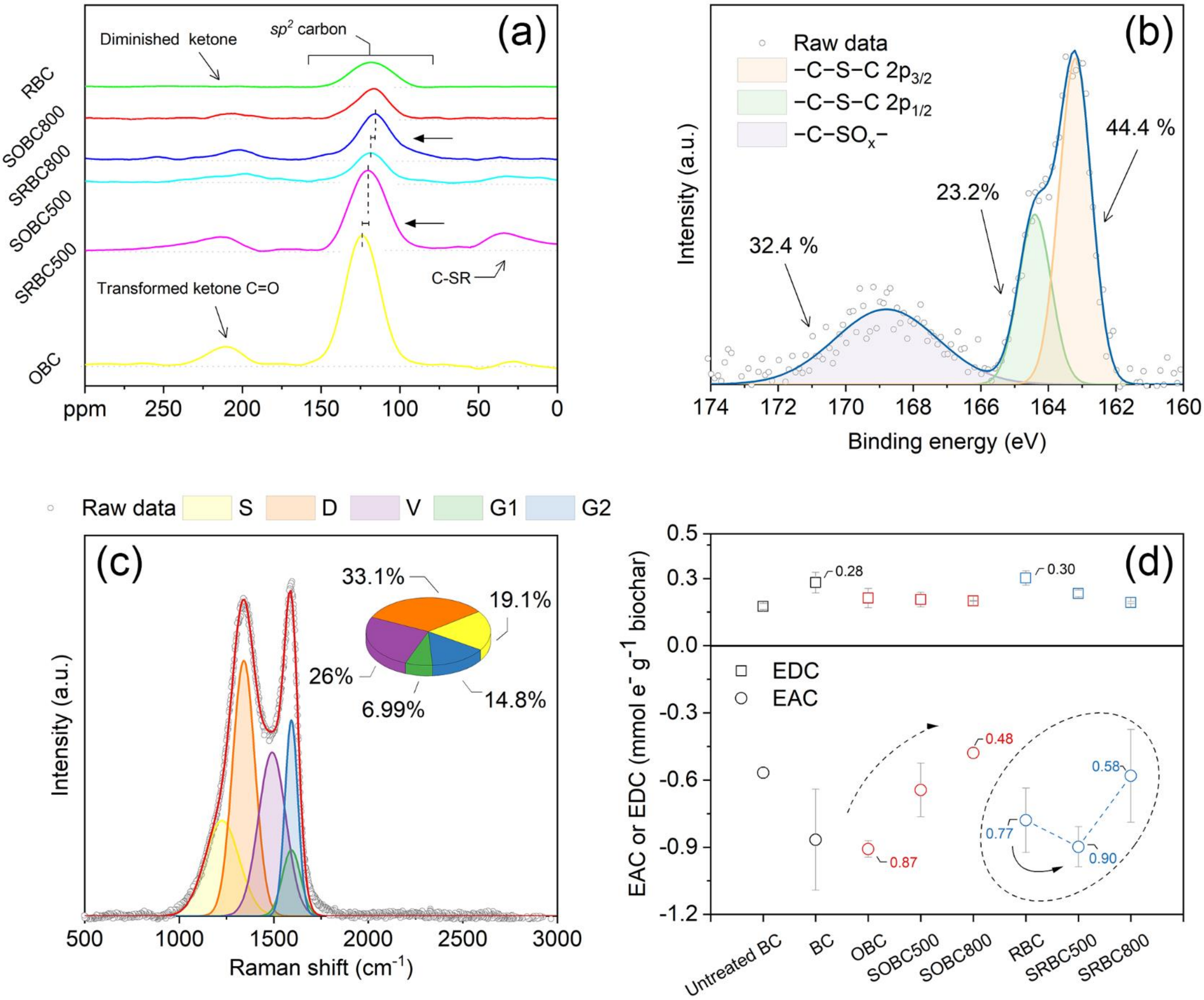

Fig. 3 ^{13}C NMR spectra of the selected biochar (a); deconvoluted XPS spectrum in S2p binding states of the SRBC500 (b); deconvoluted Raman spectrum of the SRBC500 (c); and EDC/EAC values of the selected biochar (d).

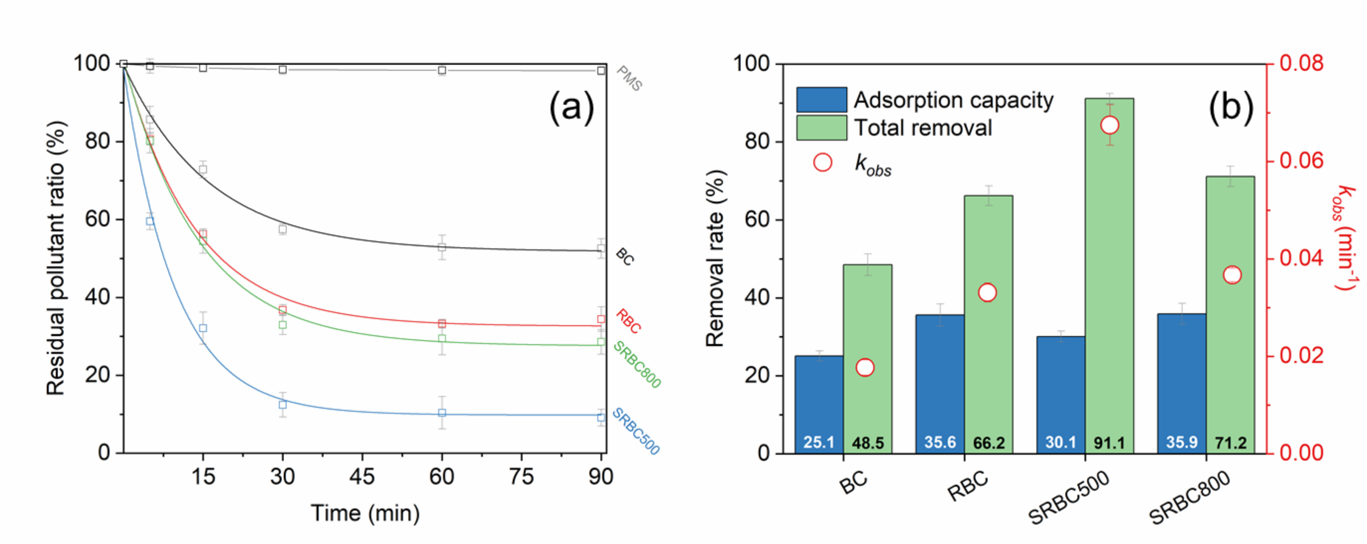

Fig. 4 Kinetics of BPA removal (R^2 = 0.98−0.99) (a) and adsorption/total removal capacities and apparent rate coefficient (b) under the different biochar/PMS systems ($[catalysts]_0$ = 0.3 g L^{-1}, $[PMS]_0$ = 3.25 mM, $[BPA]_0$ = 50 mg L^{-1}, pH_0 = 5.8 ± 0.2, T = 25 ± 1 ℃, and reaction time = 90 min).

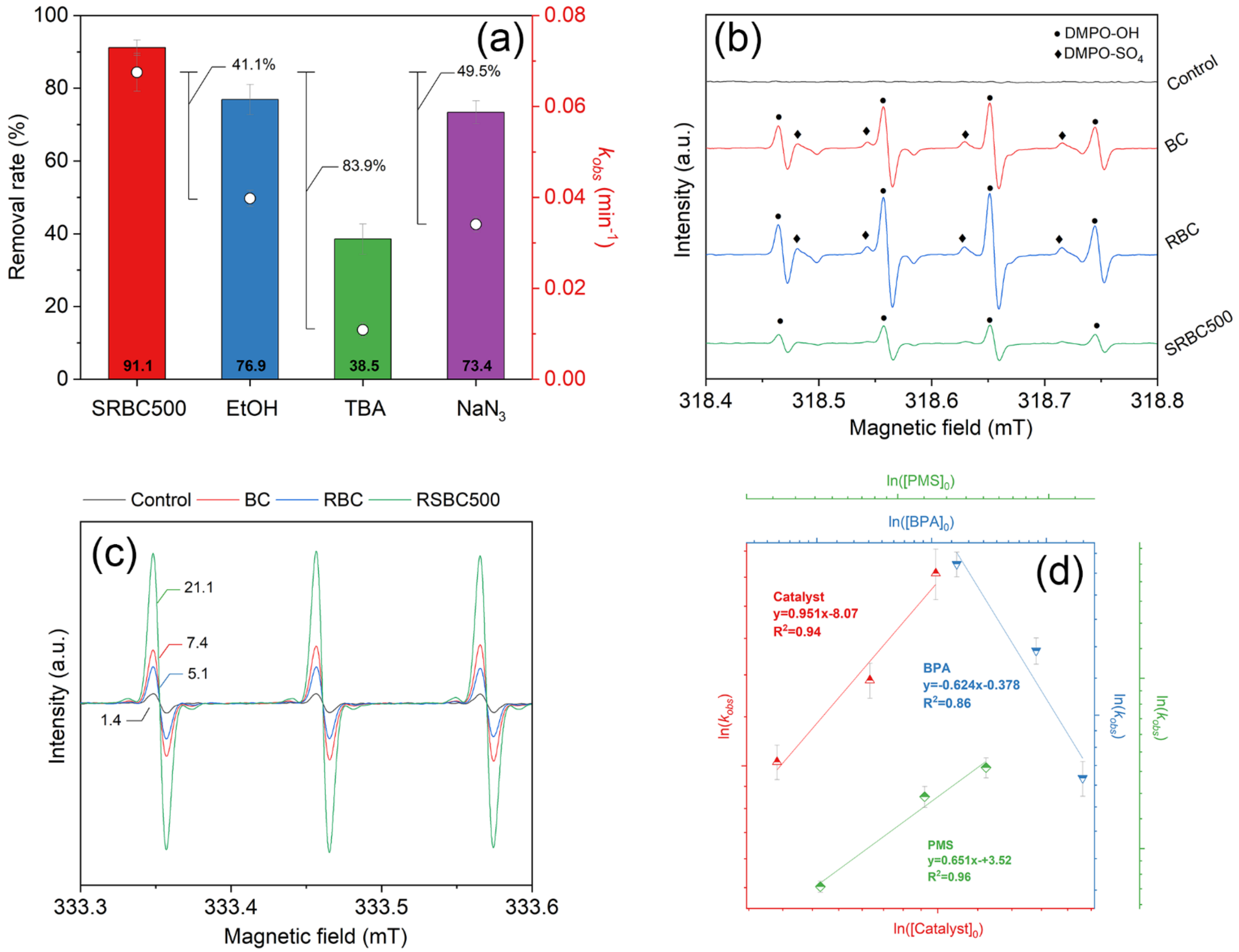

Fig. 5 Effect of different scavengers on the SRBC500 ($[\text{catalysts}]_0 = 0.3$ g L^{-1}, $[\text{PMS}]_0 = 3.25$ mM, $[\text{BPA}]_0 = 50$ mg L^{-1}, $\text{pH}_0 = 5.8 \pm 0.2$, T = 25 ± 1 ℃, $[\text{EtOH/PMS}]_0 = 500{:}1$, $[\text{TBA/PMS}]_0 = 500{:}1$, $[\text{NaN}_3/\text{PMS}]_0 = 20{:}1$, and reaction time = 30 min) (a); EPR spectra using DMPO (b) or TEMP (c) as the spin-trapping agent; and linear fittings between logarithms of k_{obs} and the varied experimental parameters (*i.e.*, catalyst dosage, PMS dosage, and BPA concentration) (d).

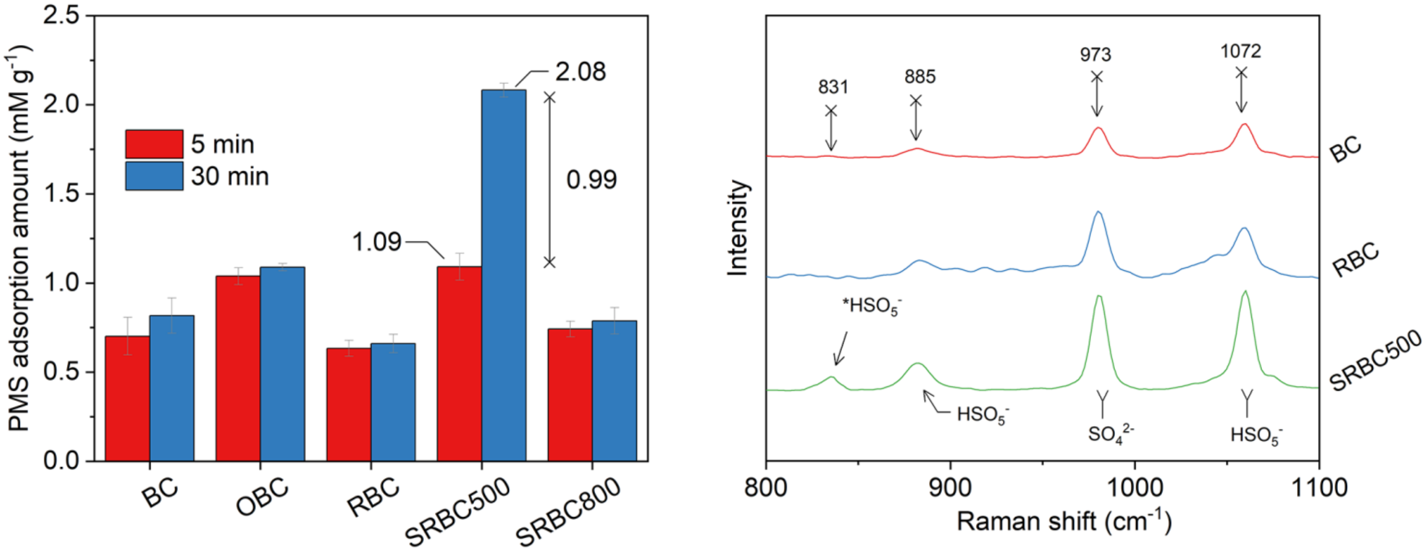

Fig. 6 PMS adsorption capacities over time (a) and *in-situ* Raman analysis (b) of the selected biochars.

Supplementary Material

Abstract

Heteroatom doping is a promising technique to enhance biochar for effective environmental remediation. However, development of electroactive heteroatom-doped biochars, *e.g.*, sulfur-doped biochar, has been hindered due to complex nature of non-stoichiometric biomass-derived carbon and changeable electrochemical state of dopants. Herein, we produced a series of platform wood-derived biochars with customized levels of minerals and redox-active moieties, aiming to unravel the crucial factors determining sulfur doping. Calcium (Ca) in biochar was found to preferentially coordinate with sulfur to form inactive inorganic sulfur minerals (*i.e.*, $CaSO_4$ and CaS) with inferior catalytic reactivity. After diminishing the inherent Ca minerals beforehand, we could introduce surface phenoxyl-type radicals ($C-O^\bullet$) and vacancy defects on the biochar to develop an electrophilic C−S−O bonding configuration, which guaranteed a high affinity towards peroxymonosulfate (PMS, 2.08 mM g^{-1}, 30 min) and efficient removal of bisphenol A (BPA, 91.1%, 30 min). Scavenging experiments and *in-situ* Raman analyses indicated that the epoxide-like C−S−O structure induced nucleophilic addition of PMS to generate surface singlet oxygen ($^1O_2$, major) and hydroxyl radicals ($^\bullet OH$, minor) through a preservative and stoichiometric interfacial reaction. Overall, the approach described overcomes the major hurdles in science-informed fabrication of sulfur-doped biochar and advances its development in niche environmental remediation.

Declaration of interests

☒ The authors declare that they have no known competing financial interests or personal relationships that could have appeared to influence the work reported in this paper.

☐The authors declare the following financial interests/personal relationships which may be considered as potential competing interests: